RESEARCH ARTICLE

ADVANCED MATERIALS
www.advmat.de

Tri-System Interlocking Top-Encased Structures Enabled Highly Stable Tin-Lead Perovskite Photodetection Arrays

Hui Liu, Tingxi Chen, Shuyan Chen, Jiayun Sun, John Jinwook Kim, Yi Yang, Guodan Wei, Yanning Zhang, and Wallace C. H. Choy**

Tin-lead binary perovskites show a very broad spectral bandwidth from ultraviolet (UV) to near-infrared (NIR) and outstanding optoelectronic properties for photodetection applications. However, the oxidation tendency of the divalent tin easily causes severe vacancies and defects, deteriorating the efficiency and stability of the device. In this work, without involving any costly synthesis of additives, a natural reducing agent of chlorogenic acid is proposed to establish a unique top-encased tri-system interlocking structure in tin-lead perovskites. Benefiting from the synergetic closed-loop interactions among functional groups of the additive with perovskites, tin-lead perovskite photodetectors (PDs) are demonstrated with improvements in energy-level alignment, antioxidation, and defect suppression and passivation. Finally, the self-powered perovskite NIR PDs present a high external quantum efficiency of ≈76%, an outstanding specific detectivity of 2×10^{13} Jones at 940 nm, and a large linear dynamic range of 222 dB, along with good stability maintaining 96% of initial photocurrent after 127 days for the unencapsulated PDs storing under N_2 atmosphere. By integrating with a 64 × 64 thin-film transistor array, the tin-lead perovskite image sensor exhibits clear and accurate imaging properties, paving the way for a wide range of high-detectivity and high-resolution imaging applications.

1. Introduction

Near-infrared (NIR) photodetection from 780 to 1800 nm presents growing promise in various applications for security, safety, and health, including security monitoring, materials identification and inspection, machine vision, light detection, and ranging, and biomedical fluorescence imaging.[1–5] Particularly, photodetection at the wavelength of 940 nm is very appealing and essential, as 940 nm illumination is a commercially available light source that is invisible and ideal for security scenarios. Efficient photodetectors (PDs) responding to 940 nm are expected to be integrated into multiple applications, such as micro gesture recognition, for future advancement.[6] Nowadays, commercially available NIR PDs primarily rely on silicon, indium gallium arsenide, and germanium, with the silicon dominating the market for a detection window within 950 nm.[7] Nevertheless, complicated and costly fabrication processes such as high temperatures and high vacuum, are required for these conventional semiconductor-based technologies. Therefore, a kind of semiconductor with NIR response that can be fabricated by simple solution processes at low temperatures into cost-effective NIR photodetectors is highly desirable.

Among the family of perovskites, tin-lead binary perovskites present narrower bandgaps from 1.5 eV to the lowest value of 1.17 eV, which enables the detection range toward the NIR region to ≈1050 nm, a comparable onset to silicon. Compared with the low absorption coefficient of silicon at NIR wavelength (≈10^2 cm^{-1} at 940 nm), tin-lead perovskites have a much stronger absorption coefficient (≈10^4 cm^{-1} at 940 nm).[8–10] Therefore, tin-lead perovskites are promising candidates as efficient NIR photodetectors. Whereas, the light absorption and photon harvest in the long-wavelength NIR range is lower than that in the visible region for tin-lead perovskites. Therefore, to achieve high-detectivity NIR photodetection, a thick tin-lead perovskite light absorber is expected to be employed to capture more long-wavelength light and enhance photogenerated carriers. A report shows that with a 1 µm-thick tin-lead perovskite layer, the photon harvesting and the external quantum efficiency (EQE) of the NIR PDs are improved.[11] According to theoretical predictions, the

---

H. Liu, J. Sun, J. J. Kim, Y. Yang, W. C. H. Choy
Department of Electrical and Electronic Engineering
The University of Hong Kong
Pokfulam Road, Hong Kong 999077, China
E-mail: chchoy@eee.hku.hk

T. Chen, Y. Zhang
Institute of Fundamental and Frontier Sciences
University of Electronic Science and Technology of China
Chengdu, Sichuan 610054, China
E-mail: yanningz@uestc.edu

S. Chen, G. Wei
Tsinghua-Berkeley Shenzhen Institute (TBSI)
Tsinghua Shenzhen International Graduate School
Tsinghua University
Shenzhen 518000, China

The ORCID identification number(s) for the author(s) of this article can be found under https://doi.org/10.1002/adma.202502191

DOI: 10.1002/adma.202502191

optimal thickness of a tin-lead perovskite film should be greater than 1 μm.[12]

However, rich defects in the thick tin-lead perovskite films caused by poor film quality normally result in high recombination of photogenerated carriers and poor device performance. We previously proposed a double-sided crystallization tuning approach to grow high-quality tin-lead perovskite thick film with a thickness of >1 μm.[13] The efficiency and responsivity of PDs at the NIR region are significantly enhanced by the high-quality thick film. Besides, vacancies caused by the oxidation of divalent tin and surface defects in tin-lead perovskites also function as recombination centers, leading to severe deterioration of device performance. To prevent the fast Sn^{2+} oxidation, reductant additives such as tin fluoride (SnF_2), metallic tin powder and wire, and gallic acid have been employed in tin-containing perovskites to combat the oxidation and decrease the trap states.[3,14–19] To reach further increased NIR photodetection, strategies for achieving superior antioxidation and surface defect passivation are highly important.

In this work, we introduce a novel chlorogenic acid (CGA) additive into the thick tin-lead perovskite system to achieve highly efficient NIR photodetection. Interestingly, CGA, as a low-cost natural reducing agent, presents a synergistic effect. The CGA and SnF_2 at the perovskite surface form a unique top-encased protection layer with a stable tri-system interlocking structure. Specifically, the CGA additive interacts with SnF_2 to produce an amorphous complex encasing in perovskite top-grain surface and boundaries, and simultaneously, CGA and SnF_2 molecules would interact with Sn^{2+}/Pb^{2+} metal ions to form a stable tri-system interlocking structure at the surface, protecting the bulk tin-lead perovskites. Benefiting from the tri-system interlocking top-encased structure, tin-lead perovskites show significantly increased antioxidation ability, improved energy-level alignment, and enhanced defect suppression. Consequently, the self-powered tin-lead perovskite NIR PDs present a high EQE of ≈76%, an outstanding specific detectivity (D^*) of 2×10^{13} Jones at 940 nm, and a large linear dynamic range (LDR) of 222 dB. Notably, the unencapsulated tin-lead perovskite PDs with the top-encased layer present significantly enhanced stability of maintaining 96% of the initial photocurrent after storing 127 days in N_2 conditions. By integration with a 64 × 64 pixelated thin-film transistor (TFT) array, the tin-lead perovskite image sensor exhibits clear and accurate imaging properties, paving the way for high-detectivity and high-resolution imaging applications.

2. Results and Discussion

2.1. Top-Encased Protection Layer with Stable Tri-System Interlocking Structure

To increase the antioxidation ability of tin-lead perovskites, we introduce three acids, including CGA, caffeic acid (CA), and quinic acid (QA), shown in **Figure** 1a, which have carboxyl and hydroxyl groups with reducing and/or coordination abilities in the MA-free $FA_{0.85}Cs_{0.15}Sn_{0.5}Pb_{0.5}I_3$ perovskite precursor. We first investigate their reducing abilities by dissolving three molecules with identical molar mass into the same $AgNO_3$ solutions to reduce Ag^+ into Ag. Since Ag particles have absorption for the light during 300–400 nm, a stronger reducing ability of the molecule would lead to more production of Ag and thus lower transmittance at 300–400 nm. As a result, we show that the CGA molecule presents the strongest reducing ability compared with CA and QA (Figure 1b).

Then, we prepare tin-lead perovskite thick films through a previously developed crystallization method,[13] and fabricate NIR PDs with a planar architecture of indium tin oxide (ITO)/poly(3,4-ethylenedioxythiophene)-poly(styrenesulfonate) (PEDOT:PSS)/$FA_{0.85}Cs_{0.15}Sn_{0.5}Pb_{0.5}I_3$/phenyl-$C_{61}$-butyric acid methyl ester (PCBM)/zirconium acetylacetonate (ZrAcac)/silver (Ag). For comparison studies, a reference device is fabricated using the pure tin-lead perovskite precursor and a basic SnF_2 additive. Detailed experimental procedures are provided in the Experimental Section. By contrasting the effect of various CGA concentrations on the device performance, the optimal amount of CGA is evaluated and proven to be trace amount of 0.5% (the percentage refers to the molar ratio of CGA to tin iodide), which aids in achieving the maximum on/off ratio for devices (Figure S1, Supporting Information). It is noted that the presence of basic SnF_2 additive is necessary. The devices show undesirable performance if they only contain optimal CGA without SnF_2 basic additive (Figure S2, Supporting Information). Therefore, we introduce optimal CGA additive into the tin-lead perovskite system with SnF_2 basic additive to achieve high-performance NIR photodetection; the detailed mechanism will be revealed later. With the same ratio of 0.5%, the antioxidation abilities of CGA, CA, and QA on perovskite films and the corresponding on/off ratios of devices are investigated. Figure 1c shows that the CGA additive has a stronger ability to keep Sn^{2+} from oxidation than CA, when QA does not show any antioxidation capability as compared with the reference (the detailed results of Sn^{2+} ratios from X-ray photoelectron spectra (XPS) tests will be explained in the next section). Moreover, PDs with CGA and CA additives achieve much higher on/off ratios (with higher photocurrent and lower dark currents) than the reference, with the CGA-based PDs being superior. However, the QA-based device shows a lower photocurrent (Figure 1d).

To understand the improvement, we first use density functional theory to investigate interactions in tin-lead perovskite systems with SnF_2 and each of the reducing agents (CGA, CA, or QA). As depicted in **Figure** 2a–c, modeling shows that the introduction of CGA molecule leads to the form of a unique closed-loop tri-system (SnF_2/CGA/tin-lead perovskites) interlocking structure, which cannot be formed by CA or QA. The binding energy of the perovskite formed by CGA (−3.413 eV) is much greater than that by CA (−1.629 eV) and QA (−1.184 eV) (Figure 2d), implying that the tri-system interlocking structure formed with CGA creates a much stable interaction to modify and protect tin-lead perovskites. The calculation equation of binding energies is described in the Supporting Information. To gain an insightful understanding of the formation of stable tri-system interlocking by CGA, we also investigate interactions between CGA and the metal sources (i.e., PbI_2, SnI_2, and SnF_2) in the initial perovskite precursor. Optimized structures and binding energies are summarized in Figure 2e. CGA bonds with metal cations through the carboxyl group, and CGA would favorably interact with SnF_2 rather than PbI_2 and SnI_2, which theoretically supports the formation of the CGA-SnF_2 complex observed experimentally (will be discussed in detail in next section.).

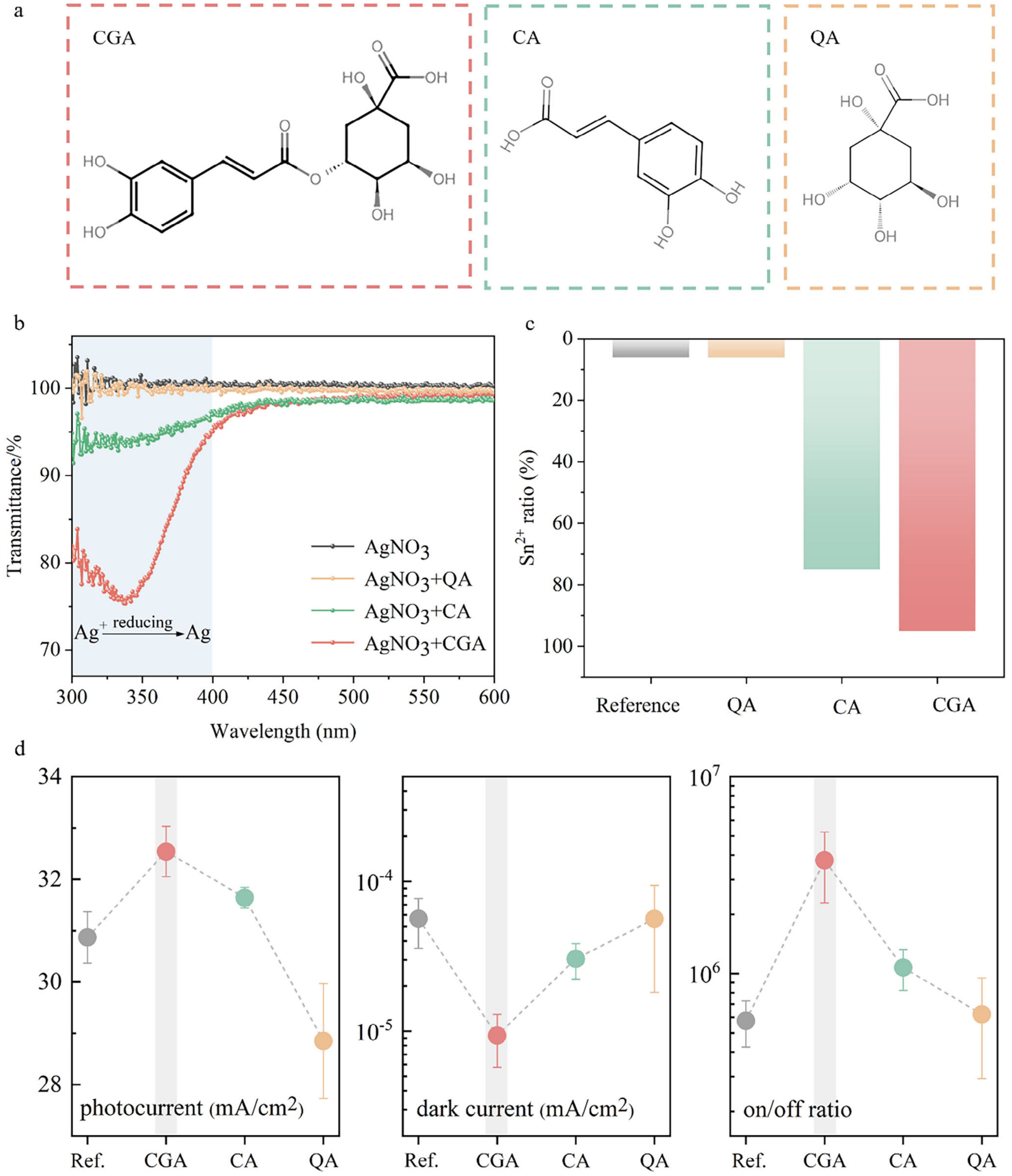

Figure 1. a) Molecules structures, and b) reducing abilities of CGA, CA and QA additives; c) Sn^{2+} ratios of tin-lead perovskite films with CGA, CA and QA; d) Comparison results of photocurrents, dark currents and on/off ratios of reference PDs and PDs with CGA/CA/QA additives.

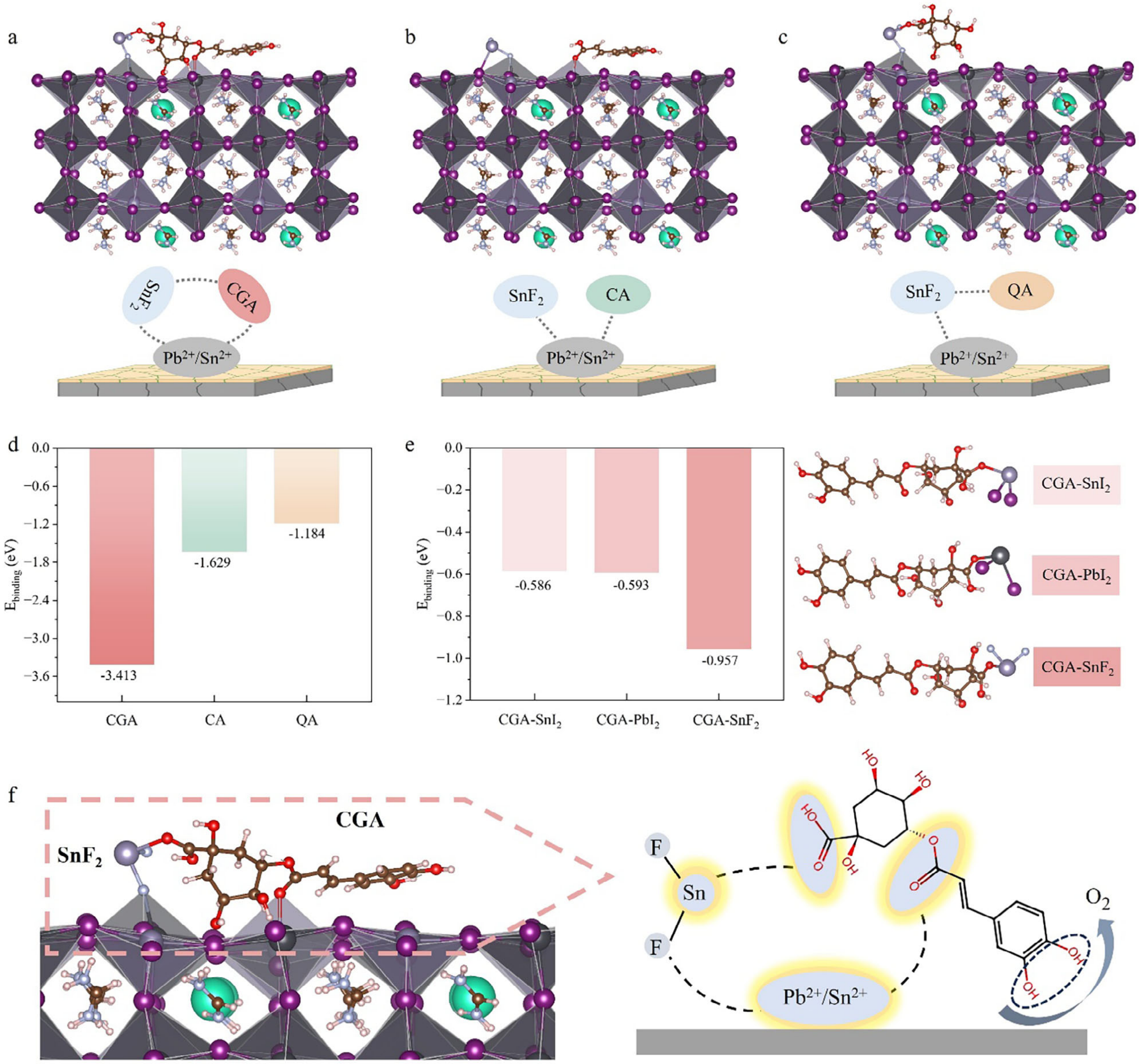

Figure 2. Modeling results of interactions in tin-lead perovskite systems with the presence of basic SnF_2 additive and a) CGA, b) CA, and c) QA additives. The red, light purple, light black, and blue, spheres denote O, Sn, Pb and F, respectively; d) binding energies in the perovskite system with CGA, CA or QA; e) Optimized structures and binding energies of CGA with PbI_2, SnI_2, and SnF_2; f) Scheme diagram of the tri-system synergetic interaction of CGA with tin-lead perovskites surface.

Moreover, to study the absorption trend of CGA with metal cations at the perovskite surface, we examine the (001) SnI_2/PbI_2 terminated $FA_{0.85}Cs_{0.15}Sn_{0.5}Pb_{0.5}I_3$ surface (Figure S3, Supporting Information). The binding energy of CGA with Pb^{2+} site is −1.660 and −1.759 eV for Sn^{2+} site, indicating that CGA would prefer to interact with Sn^{2+} in the tin-lead perovskite surface. It is noted that the formation energy of prevalent defects in tin-lead perovskites centered with Sn^{2+} ($V_I(Sn)$) is 0.073 eV lower than that centered with Pb^{2+} ($V_I(Pb)$) (Figure S4, Supporting Information), which suggests that most of the undercoordinated metal sites in the tin-lead binary perovskite film surface would be Sn^{2+} instead of Pb^{2+}. Therefore, the preferred interaction of CGA additive with Sn^{2+} in the tin-lead perovskite would contribute to passivating the tin-related defects and effectively preventing the oxidation of tin content. Consequently, the CGA additive interacts with SnF_2 to form the CGA-SnF_2 complex through the binding of carboxyl group and Sn^{2+}, and the ester group of CGA would simultaneously favorably bond to Sn^{2+} metal ions of tin-lead perovskites and the F^- of SnF_2 interact with nearby Pb^{2+} of perovskites, which ultimately create a stable tri-system interlocking structure (Figure 2f).

We then experimentally study the influence of CGA on tin-lead perovskites, in which $FA_{0.85}Cs_{0.15}Sn_{0.5}Pb_{0.5}I_3$ perovskite with basic SnF_2 and optimal CGA additives is named as the target film,

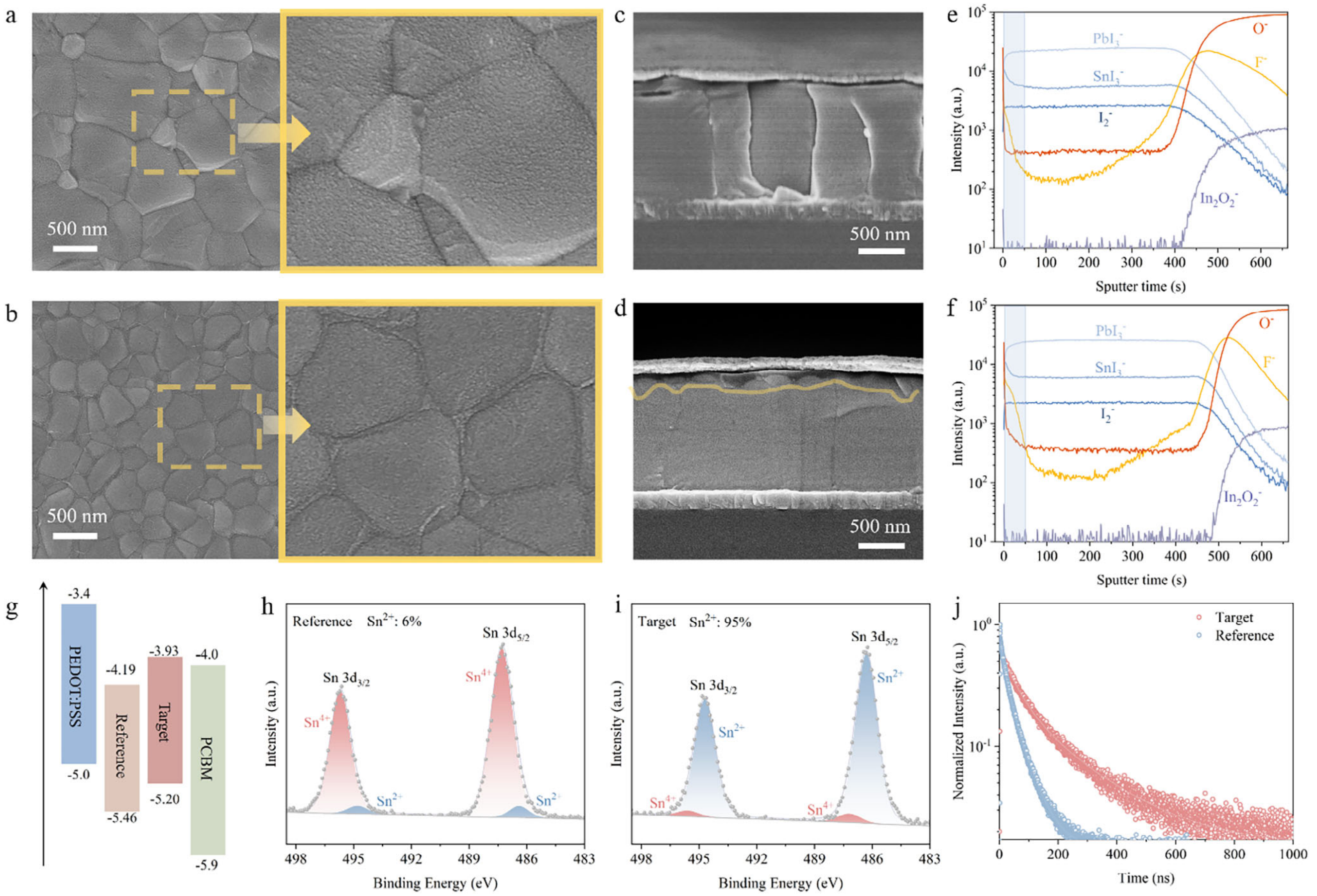

Figure 3. SEM with regional enlarged images a,b) and cross-sectional SEM c,d) of reference and target tin-lead perovskite films, respectively; TOF-SIMS depth profiles of e) reference, f) target tin-lead perovskite samples with a structure of perovskite film/PEDOT:PSS/ITO; g) energy alignment diagram; Sn 3d XPS spectra of h) reference, i) target perovskites; j) TRPL of reference and target perovskites, structures of tested samples are quartz substrate/perovskite film.

and the perovskite with basic SnF_2 only is marked as a reference. With the CGA additive, the morphology of target film is significantly different from that of the reference. As shown in scanning electron microscope (SEM) images in **Figure** 3a,b, the surface of reference film comprises both large and small grains, with a rms roughness of 29 nm (Figure S5a, Supporting Information). Distinctively, the target perovskites show relatively smaller, but more uniform and smoother gains distribution at the film surface. The roughness of the target perovskite surface is significantly reduced to 19 nm (Figure S5b, Supporting Information). Interestingly, in the target perovskite film, an amorphous complex is observed distributing in the top grain surface and boundaries to encase perovskite grains, which is absent in the reference film. From the cross-sectional SEM, a thin top region containing smaller grains (≈1/10 of the whole perovskite film) is visible (Figure 3d), consistent with the characteristic surface with a smaller-grain distribution in SEM. The perovskite grains underneath the region are not influenced and remain comparable to those in the reference (Figure 3c). To further validate the influence of CGA additives on morphology, the tin-lead perovskite film with a higher additive concentration (i.e., 1%) is also characterized. The impact of the complex on the top surface of perovskites becomes more pronounced when additive concentration is increased (Figure S6, Supporting Information). The small grains and boundaries of the surface are enveloped by more complex structures, and the top region with the complex becomes wider with the higher concentration of CGA.

We then investigate the element distribution of reference and target tin-lead perovskite films, as shown in Figure 3e,f. The CGA additive is tracked by its characteristic O element, which is absent for perovskites. In the reference sample (Figure 3e), O signals are absent in the whole tin-lead perovskite film, except for a high O signal at the sample surface. A completely identical intensity of O signal is also detected in the target perovskite sample surface (Figure 3f), which indicates that the surface O signals in both samples can be explained by the absorbed oxygen from the air, due to the inevitable exposure to the air atmosphere during the preparation of samples. Meanwhile, both samples exhibit the same rise of O signals after perovskite films, which originates from the sub-layers (i.e., PEDOT: PSS and ITO) of the samples. Regardless of the surface absorbed oxygen and O signals in PEDOT: PSS and ITO layers, a distinguishing difference between reference and target perovskite films is that O signals present existence in a short depth of the top region (denoted by a light-blue rectangle) in the target perovskite film, which is absent in reference film. The depth of this top region is ≈1/10 of the whole tin-lead perovskite film, corresponding to the thickness of the thin top layer with small perovskite grains encased by a complex observed in morphology. Moreover, within the same top region (i.e., the region marked with the light-blue rectangle), the F signal from SnF_2 in the target film shows higher intensity than that in the reference film. Therefore, we infer that the introduced CGA additive could interact with SnF_2 to form an amorphous complex,[15,17,20] that encases the perovskite top grain surface and boundaries. Overall, compared with reference tin-lead perovskites, a top-encased protection layer is built in the target perovskite film to effectively prevent oxidation and defect generation (Figure S7, Supporting Information).

To prove this speculation, we prepare the SnF_2 and CGA-SnF_2 complex samples by dissolving SnF_2 and CGA/SnF_2 mixed powders in DMF and DMSO mixed solutions, respectively, then depositing materials on the glass substrates before drying. As indicated in Figure S8 (Supporting Information), XRD patterns show that the crystalline SnF_2 is transformed into an amorphous phase after interacting with the CGA additive. Furthermore, the crystal particles of SnF_2 materials are observed in the SnF_2 film, but the film formed by mixed CGA-SnF_2 presents a smooth and homogeneous amorphous morphology, which is consistent with the results in XRD. Interestingly, mixed samples of "SnI_2+CGA" and "PbI_2+CGA" prepared under the same conditions still keep the crystal peaks of SnI_2 and PbI_2, respectively, and present morphologies of particles, although intensities of XRD peaks and shapes of particles have some changes due to the mixture of CGA. These results suggest that the CGA molecule prefers to interact with SnF_2 rather than PbI_2 and SnI_2, which is consistent with the outcome of theoretical studies and confirms the formation of the CGA-SnF_2 complex. The reference and target tin-lead films show identical absorption onsets, and both films exhibit the same characteristic XRD peaks matching the pseudo-cubic structure of tin-lead perovskites (Figure S9, Supporting Information), indicating that CGA does not change the bandgap and crystal structure of perovskites. Therefore, according to the above results, it can be concluded that the introduced optimal CGA additive would interact with SnF_2 to form a CGA-SnF_2 complex passivating perovskites top grains in surface and boundaries through stable tri-system interlocking to create a thin top-encased protection layer, which would potentially influence the electrical property of film surface, effectively preventing the tin oxidation, as well as suppressing and passivating defects.

Ultraviolet photoelectron spectroscopy (UPS) is used to analyze the energetics of tin-lead perovskite films. Figure 3g shows the energy alignment diagram with band values of reference and target perovskites, and secondary electron cut-off and valence band edge spectra of perovskites are presented in Figure S10 (Supporting Information). The valence band maximum (VBM) locations of reference and target perovskites are −5.46 and −5.20 eV, respectively, following the equation of $E_{VBM} = 21.22 - (E_{cutoff} - E_{onset})$.[21] By the bandgap of 1.25 eV of both films (Figure S9, Supporting Information), the conduction band minimum (CBM) values of perovskites are determined. Clearly, the top-encased protection layer with tri-system interlocking by the introduction of CGA additive alters the electronic structure of the perovskite surface of upshifting CBM from −4.19 eV (reference) to −3.93 eV (target), leading to improved energy level alignment and favorable energetics for electron extraction and transfer between perovskites layer and electron transport layer.

Furthermore, the antioxidation ability of tin-lead perovskites by the introduction of CGA additive is examined. We first investigate the function of CGA additives in the perovskite precursor (Figure S11, Supporting Information). When the reference perovskite precursor is exposed to air, it quickly becomes red due to the oxidation of Sn^{2+} to Sn^{4+}. However, the target perovskite precursor evolves at a slower speed, indicating that, as a natural reducing agent, CGA can effectively help prevent the oxidation of tin-lead perovskite precursor. Then, XPS is employed to determine the degree of oxidation in tin-lead perovskite films. The reference exhibits a Sn^{2+} percentage of 6% (Figure 3h). Surprisingly, the Sn^{2+} ratio in the target film is greatly increased to 95% (Figure 3i). It is noted that CA shows a facilitated antioxidation effect but is weaker than CGA (Figure S12, Supporting Information), and QA does not offer any antioxidation ability (Figure S13, Supporting Information). The significantly enhanced antioxidation effect by the introduction of CGA is contributed by the formation of top-encased protection layer with stable tri-system interlocking and the reducing phenolic hydroxyl groups of CGA acting as oxygen scavengers.[22] The largely suppressed oxidation contributes to the reduction of defects, leading to decreased nonradiative recombination.

To investigate the charge carrier behavior in reference and target perovskite films, steady-state photoluminescence (PL) and time-resolved PL (TRPL) measurements are employed. The PL intensity of the target perovskite film is higher than that of the reference film (Figure S14, Supporting Information), indicating the effectively decreased defects in the film. Figure 3j shows the time-resolved TRPL spectra of perovskite films. A bi-exponential decay mode is used to fit the TRPL curves, and fitting parameters are listed in Table S1 (Supporting Information). The fast decay (τ_1) and slow decay (τ_2) are attributed to the surface trap-assisted recombination and the radiative recombination in the bulk crystals, respectively.[23,24] In comparison to the τ_1 of reference perovskites (16.43 ns), the target perovskite film displays a slower trapping time of 51.83 ns, which is ascribed to the suppression and passivation of defects by the top-encased protection layer with stable tri-system interlocking. Moreover, τ_2 is prolonged from 52.31 ns (reference) to 200.50 ns (target), revealing that the bulk of target perovskites is effectively protected from oxidation, thus achieving decreased defect density and nonradiative recombination. Furthermore, trap densities of perovskite films are studied by the space charge-limited current (SCLC) characterization (Figure S15, Supporting Information). Deriving from dark current-voltage curves of the hole-only devices, a lower trap-filled limit voltage (V_{TFL}) of 0.123 V is obtained in the target perovskite-based device, in comparison to that of the reference device (0.155 V). The trap density is proportional to the V_{TFL}.[25] As a result, the target perovskite-based device shows a lower trap density of 3.59×10^{14} cm^{-3} than the reference perovskite device (4.53×10^{14} cm^{-3}), confirming the decreased defects in the target tin-lead perovskite film by the introduction of CGA additive.

Electrochemical impedance spectroscopy (EIS) is employed to study the charge transfer and recombination kinetics inside the perovskite PDs. Nyquist plots of PDs with an inserted equivalent circuit are illustrated in Figure S16 (Supporting Information), and the fitting parameters comprising series resistance (R_s) and recombination resistance (R_{rec}) are listed in Table S2 (Supporting Information). In the reference PD, the fitted R_s and R_{rec} are 16.97 and 1833 Ω, respectively. Surprisingly, the target perovskite PD shows a lower R_s of 13.78 Ω and a higher R_{rec} of 2941 Ω. The decreased R_s indicates the improved charge transfer, benefiting from the improved energy-level alignment. Meanwhile, the significantly increased R_{rec} demonstrates the diminished charge recombination due to the defect passivation and oxidation suppression by the top-encased protection layer.

2.2. High-Performance PDs with the Top-Encased Protection Layer

The current density–voltage curves (*J*–*V* curves) of reference and target tin-lead perovskite PDs are depicted in Figure S17 (Supporting Information). The target PD presents a substantially decreased dark current of 1.03×10^{-7} mA cm^{-2} at zero bias, which is almost one order of magnitude lower than the reference PD. This result shows that the decreased trap density and leakage current are due to the enhanced defects passivation and antioxidation by the top-encased protection layer with a stable tri-system interlocking structure in the presence of CGA. Meanwhile, the target PD exhibits improved EQE from visible to NIR region compared with the reference PD, with values exceeding 80% among 780–905 nm, and a high value of 75.6% at 940 nm (Figure S18a, Supporting Information). In addition, the target PD presents a high responsivity (R) of 0.57 A W^{-1} at 940 nm (Figure S18b, Supporting Information). The enhanced EQE and R are ascribed to improved carrier transport and collection within the device.

Moreover, the noise current (i_n) is another important parameter determining the detectivity of PDs. In general, the noise current comprises shot noise (i_{shot}), thermal noise ($i_{thermal}$), and flicker noise (1/f noise).[26] The former two are frequency-independent, whereas flicker noise is frequency-dependent. The shot noise and thermal noise are expressed as the following equations, respectively.

$$i_{shot} = \sqrt{2eI_dB} \tag{1}$$

$$i_{thermal} = \sqrt{\frac{4KTB}{R_{shunt}}} \tag{2}$$

where I_d is the dark current and B is the response bandwidth, k is Boltzmann's constant, T is the temperature, and R_{shunt} is the shunt resistance of the device. With the acquired i_{shot} and $i_{thermal}$, the white noise can be given as follows:

$$i_{white} = \sqrt{{i_{shot}}^2 + {i_{thermal}}^2} \tag{3}$$

The total noise currents of PDs are yielded from the fast Fourier transform of dark current as a function of time measured under zero bias (Figure S19, Supporting Information). The target PD presents largely decreased noise and is barely dependent on the frequency after 1 Hz. The measured noise current of target PD is 7.64×10^{-15} A Hz$^{-1/2}$, which is close to the calculated i_{white} of 7.41×10^{-15} A Hz$^{-1/2}$. The decreased noise of target PD and its weak dependency on the low frequency indicate the effective defect suppression by CGA. In addition, noise equivalent power (NEP) is a parameter that demonstrates the lowest incident light power that PDs can differentiate from noise current, given by the following equation.

$$\mathrm{NEP} = \frac{i_n}{R} \tag{4}$$

As shown in Figure S20 (Supporting Information), the target PD presents a significantly lower NEP than the reference PD from the visible to NIR range. A much lower NEP of 1.3×10^{-14} W Hz$^{-1/2}$ is obtained at 940 nm for the target PD, which implies that it can detect the NIR light as weak as ≈0.2 pW cm^{-2}. Furthermore, the specific detectivity (D^*) is a crucial metric that reflects the detecting capability of PDs for weak optical signals, which is obtained based on the following formula.

$$D^* = \frac{\sqrt{AB}}{\mathrm{NEP}} = \frac{R\sqrt{AB}}{i_n} \tag{5}$$

where A is the detection area of the PD. As illustrated in **Figure** 4a, benefiting from the improved responsivity and largely suppressed noise current, the target PD presents much-increased D^* from visible to NIR region in comparison to the reference PD and achieves a high D^* of 2×10^{13} Jones at 940 nm. The significantly enhanced D^* is closely related to the improved charge carrier transport, reduced nonradiative recombination, and decreased oxidation and trap states by the formation of the top-encased protection layer. The D^* of the target PD is superior to those reported tin-lead perovskite NIR PDs (Figure 4b),[3,13,19,27–32] which indicates its great potential in applications of NIR photodetection. Moreover, the detection capability of PDs over a wide range of incident light intensities is evaluated by a metric of linear dynamic range (LDR), which is defined as follows.

$$\mathrm{LDR} = 20\log\frac{P_{max}}{P_{min}} \tag{6}$$

where P_{max} and P_{min} are the maximum and minimum limitations of incident light intensity in a linear range, respectively. The LDR of reference and target PDs are measured under varied light intensities of monochromatic 940 nm light illumination, as illustrated in Figure 4c. In comparison to the reference PD, the target PD shows a lower minimum limit of incident light intensity that can be detected, at ≈0.75 pW cm^{-2}. The reduced detection limit of target PD is attributed to the largely suppressed noise current. The upper linear limit is determined by the saturation current when light intensity approaches a certain level,[33] and the measured maximum incident light intensity is 10^{-1} W cm^{-2} in our case. Consequently, the target PD exhibits an LDR of 222 dB, which is larger than that of inorganic silicon PDs (≈120 dB) and InGaAs PDs (66 dB).[34] The result indicates the great detection potential of optimized PD in a wide range.

The response speed is an essential figure of merit that measures the ability of PDs to respond to rapidly changing optical signals. It is tracked by the transient photocurrent (TPC) response measurement with a 6 ps pulse laser under zero bias. Typically, the response speed comprises rise and fall time, which is defined as the time interval of the photocurrents varying between 10%

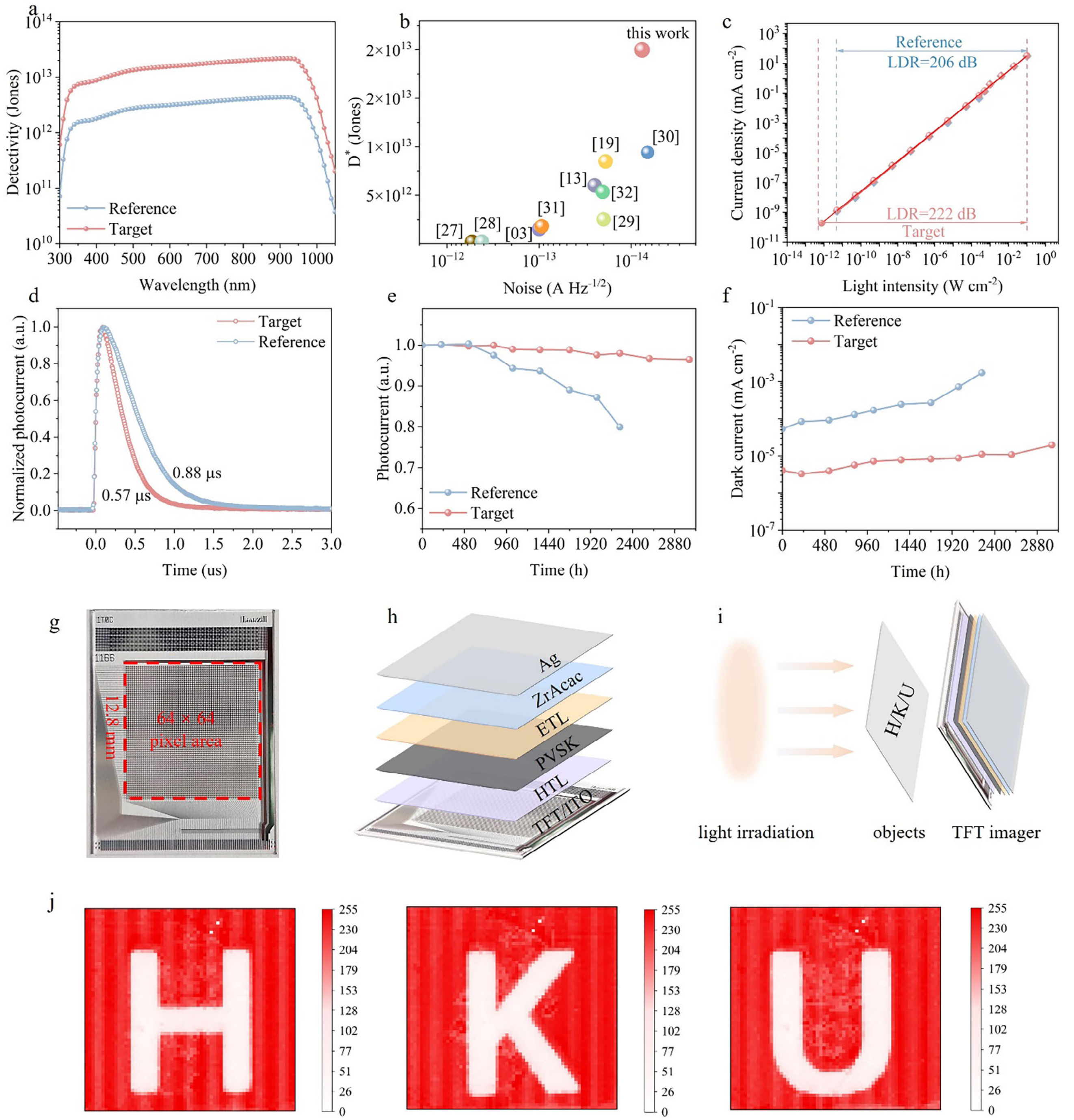

Figure 4. a) specific detectivity spectra of PDs; b) device performance comparation of reported tin-lead perovskite PDs and this work; c) LDR plots, d) transient photocurrent response of reference and target PDs; Stability of e) normalized photocurrent density and f) dark current density at −100 mV of unencapsulated PDs stored at N_2 atmosphere; g) photo image of the TFT array of 64 × 64 TFT backplane; Schematic diagrams of h) perovskite-TFT imager, i) imaging process; j) imaging results of letters "H", "K" and "U" by target tin-lead perovskite imager.

and 90% of the maximum value. As shown in Figure 4d, the target PD presents a faster response speed than that of the reference PD (0.88 μs), showing a shorter fall time of 0.57 μs. The enhanced response speed is attributed to the improved charge transport and suppressed defects by the CGA complex-enabled top-encased layer. Further minimizing device area will increase the response speed.[3,35]

The stabilities of reference and target perovskite PDs are tracked by recording their photocurrent densities and dark current densities under −100 mV, and devices are unencapsulated and stored in an N_2 atmosphere. As shown in Figure 4e,f, the target PD presents significantly improved stability than the reference PD. After storing for 127 days, the photocurrent of the target PD shows a slight degradation and eventually maintains 96% of the initial value. However, after storing 94 days, the photocurrent of the reference PD has already attenuated to below 80% of its original value. Meanwhile, compared to the obvious enhancement of the dark current in the reference PD, the dark current of the target PD shows a slight increase, with value changes from the initial 4.05×10^{-6} to the final 1.96×10^{-5} mA cm^{-2} after 127 days. The significantly prolonged stability of PDs is contributed by the significantly enhanced antioxidation ability and defects suppression/passivation by the complex-enabled top-encased protection layer for the tin-lead perovskite active layer.

We integrated the perovskite photodiode with a thin-film transistor (TFT) using the tin-lead perovskite with the top-encased protection layer. As shown in the schematic view in Figure 4g–i, the perovskite TFT imager is constructed in a layer sequence of the TFT and the tin-lead perovskite photodiode. The active area of the TFT array is 12.8×12.8 mm^2, and the imaging resolution is 64 × 64 with a pixel pitch of 200 µm. The imaging system works in transmission mode, where the incident light transmits through the target object and reaches the TFT array, and is further responded to by the perovskite PDs, followed by gray-scale imaging data collected through the readout circuit. We investigate the image uniformity of 4096 pixels by acquiring its imaging properties under room light irradiation. As shown in Figure S21 (Supporting Information), the perovskite array shows uniform imaging with a narrow statistical distribution of normalized photocurrent from 0.8 to 1, indicating the good uniformity of the tin-lead perovskite imager. Finally, through transmitting different objects of letters, the perovskite array can accurately recognize letters of "H", "K", and "U" (Figure 4j), which originates from the excellent performance of tin-lead perovskite PDs by the formation of a top-encased protection layer with stable interlocking interaction.

3. Conclusion

In conclusion, we employ a novel reducing agent of CGA in the tin-lead perovskite system to achieve a significantly enhanced NIR photodetector. Interestingly, CGA would interact with SnF_2 in tin-lead perovskites to form a CGA-SnF_2 complex, which simultaneously interacts with Sn^{2+}/Pb^{2+} metal ions of the perovskite to create a top-encased protection layer with a stable tri-system interlocking structure in the perovskite top grain surface and boundaries. Contributed by the functional reducing groups of CGA and the unique top-encased protection layer, the target tin-lead perovskite film shows improved energy-level alignment with facilitating carrier transport, enhanced antioxidation ability, and increased defects suppression and passivation. As a result, the self-powered tin-lead perovskite NIR PDs exhibit a high EQE of ≈76% and a remarkable D^* of 2×10^{13} Jones at 940 nm, a fast response speed of 0.57 µs, and a large LDR of 222 dB. Moreover, the unencapsulated tin-lead perovskite PD with the top-encased layer presents significantly improved stability of keeping 96% of the initial photocurrent, after storing for 127 days under N_2 conditions. Consequently, a 64 × 64 array integrated with the target tin-lead perovskites demonstrates clear and accurate imaging properties, showing the potential for high-detectivity and high-resolution imaging applications.

4. Experimental Section

The Formation of Tin-Lead Perovskite Films: First, 2 M $FA_{0.85}Cs_{0.15}Sn_{0.5}Pb_{0.5}I_3$ precursors was prepared by mixed stoichiometric amounts of formamidinium iodide (FAI, GreatCell Solar Limited, 99.99%), cesium iodide (Sigma Aldrich, 99.999%), tin iodide (SnI_2, Advanced Election Technology, 99.999%), lead iodide (PbI_2, TCI, 99.99%), and tin fluoride (SnF_2, Sigma Aldrich, 99%) into 1 mL N,N-dimethylformamide (DMF, Acros, 99.8%, extra dry) and dimethylsulfoxide (DMSO, Acros, 99.7+%, extra dry) mixed solution. For the target perovskites, a certain amount of CGA additive was added to the above precursor solution. After totally dissolving the precursors and filtering with 0.22 µm PTFE filters, the precursor solutions were spun at 2000 rpm for 30 sec, and 300 µL of antisolvent toluene was dripped onto the film at the 25th s. Then, films were annealed at 60 °C for 6 min covered by a 9 cm petri dish, and then annealed at 120 °C for 5 min.

Device Fabrication: ITO glass substrates were cleaned with detergent water, deionized water, acetone, and ethanol for 10 min, respectively, before drying with nitrogen gas blowing. Then, the ITO substrates were exposed to an ultraviolet-induced ozone atmosphere for ≈30 min. Afterward, the PEDOT:PSS (Clevios P VP Al 4083) layer was spun on the substrate at 4000 rpm for 30 s, followed by an annealing process of 140 °C for 20 min. The above processes were finished in the air atmosphere. Then, the prepared samples were transferred into the glove box filled with N_2, tin-lead perovskite layer was deposited on PEDOT:PSS substrates following the above method. Afterward, 20 mg mL^{-1} PCBM/CB solution was spun on the perovskite films at 1200 rpm, and then 2 mg mL^{-1} ZrAcac/IPA was dynamically spun at 3000 rpm. Finally, a 140 nm Ag electrode was formed by thermal deposition under a vacuum of 10^{-6} Torr. The active area of PDs was 0.08 cm^2.

Supporting Information

Supporting Information is available from the Wiley Online Library or from the author.

Acknowledgements

This research is supported by the project of the University Grant Council of the University of Hong Kong (grant No. 202111159113, 2302101786), General Research Fund (grant Nos. 17200823, 17200021, and 17310624) from the Research Grants Council of Hong Kong Special Administrative Region, China, and Innovation and Technology Fund (GHP/245/22SZ) from Innovation and Technology Commission of Hong Kong Special Administrative Region, China. The authors also acknowledge the help of Mr. Haoquan Liang from Prof. Yanning Zhang's group for their modeling work.

Conflict of Interest

The authors declare no conflict of interest.

Data Availability Statement

The data that support the findings of this study are available from the corresponding author upon reasonable request.

Keywords

chlorogenic acid, near-infrared photodetector, Tin-lead perovskites, top-encased tri-system interlocking

Received: February 1, 2025
Revised: May 31, 2025
Published online:

[1] J. Guo, C. Chen, C. Chen, E. Zuo, B. Dong, X. Lv, W. Yang, *Sci. Rep.* **2022**, *12*, 7928.
[2] S. Kogou, G. Shahtahmassebi, A. Lucian, H. Liang, B. Shui, W. Zhang, B. Su, S. van Schaik, *Sci. Rep.* **2020**, *10*, 19312.
[3] A. Morteza Najarian, M. Vafaie, A. Johnston, T. Zhu, M. Wei, M. I. Saidaminov, Y. Hou, S. Hoogland, F. P. García de Arquer, E. H. Sargent, *Nat. Electron.* **2022**, *5*, 511.
[4] G. Hong, A. L. Antaris, H. Dai, *Nat. Biomed. Eng.* **2017**, *1*, 0010.
[5] J. Liu, P. Liu, D. Chen, T. Shi, X. Qu, L. Chen, T. Wu, J. Ke, K. Xiong, M. Li, H. Song, W. Wei, J. Cao, J. Zhang, L. Gao, J. Tang, *Nat. Electron.* **2022**, *5*, 443.
[6] Q. Zhang, Y. Cao, H. Chen, F. Li, S. Yang, Y. Wang, Z. Yang, Y. Liu, *IEEE 40th International Conference on Distributed Computing Systems (ICDCS)* **2020**, 552.
[7] G. Konstantatos, *Nat. Commun.* **2018**, *9*, 5266.
[8] Z. M. Beiley, A. P. Abraham, E. Hanelt, B. Chen, A. Kuznetsov, N. Kolli, E. H. Sargent, *Optical Components and Materials XIV* **2017**, *10100*, 234.
[9] A. Green Martin, J. Keevers Mark, *Prog. Photovoltaics* **1995**, *3*, 189.
[10] L. Mei, R. Huang, C. Shen, J. Hu, P. Wang, Z. Xu, Z. Huang, L. Zhu, *Adv. Opt. Mater.* **2022**, *10*, 2102656.
[11] W. Wang, D. Zhao, F. Zhang, L. Li, M. Du, C. Wang, Y. Yu, Q. Huang, M. Zhang, L. Li, J. Miao, Z. Lou, G. Shen, Y. Fang, Y. Yan, *Adv. Funct. Mater.* **2017**, *27*, 1703953.
[12] W. Zhang, L. Huang, W. Zheng, S. Zhou, X. Hu, J. Zhou, J. Li, J. Liang, W. Ke, G. Fang, *Nano Energy* **2022**, *96*, 107078.
[13] H. Liu, H. L. Zhu, Z. Wang, X. Wu, Z. Huang, M. R. Huqe, J. A. Zapien, X. Lu, W. C. H. Choy, *Adv. Funct. Mater.* **2021**, *31*, 2010532.
[14] L. Ma, F. Hao, C. C. Stoumpos, B. T. Phelan, M. R. Wasielewski, M. G. Kanatzidis, *J. Am. Chem. Soc.* **2016**, *138*, 14750.
[15] S. J. Lee, S. S. Shin, Y. C. Kim, D. Kim, T. K. Ahn, J. H. Noh, J. Seo, S. I. Seok, *J. Am. Chem. Soc.* **2016**, *138*, 3974.
[16] R. Lin, K. Xiao, Z. Qin, Q. Han, C. Zhang, M. Wei, M. I. Saidaminov, Y. Gao, J. Xu, M. Xiao, A. Li, J. Zhu, E. H. Sargent, H. Tan, *Nat. Energy* **2019**, *4*, 864.
[17] T. Wang, Q. Tai, X. Guo, J. Cao, C. K. Liu, N. Wang, D. Shen, Y. Zhu, C. S. Lee, F. Yan, *ACS Energy Lett.* **2020**, *5*, 1741.
[18] S. Hu, M. A. Truong, K. Otsuka, T. Handa, T. Yamada, R. Nishikubo, Y. Iwasaki, A. Saeki, R. Murdey, Y. Kanemitsu, A. Wakamiya, *Chem. Sci.* **2021**, *12*, 13513.
[19] H. Liu, L. Zhu, H. Zhang, X. He, F. Yan, K. S. Wong, W. C. H. Choy, *ACS Energy Lett.* **2022**, *8*, 577.
[20] Y. Xing, Z. Deng, T. Guo, Z. Zhang, Q. Tai, R. Zhao, J. Xiong, Q. Wang, L. Huang, X. Liu, Z. Hu, Y. Zhu, J. Zhang, *Chem. Eng. J.* **2023**, *462*, 142122.
[21] H. Liu, J. Sun, H. Hu, Y. Li, B. Hu, B. Xu, W. C. H. Choy, *ACS Appl. Mater. Interfaces* **2021**, *13*, 45059.
[22] M. Parcheta, R. Swislocka, S. Orzechowska, M. Akimowicz, R. Choinska, W. Lewandowski, *Materials (Basel)* **2021**, *14*, 1984.
[23] T. H. Han, J. W. Lee, C. Choi, S. Tan, C. Lee, Y. Zhao, Z. Dai, N. De Marco, S. J. Lee, S. H. Bae, Y. Yuan, H. M. Lee, Y. Huang, Y. Yang, *Nat. Commun.* **2019**, *10*, 520.
[24] L. Zhang, M. Zhou, Z. Zhang, J. Yuan, B. Li, W. Wen, J. Tian, *J. Mater. Chem. A* **2019**, *7*, 22229.
[25] K. Xiao, R. Lin, Q. Han, Y. Hou, Z. Qin, H. T. Nguyen, J. Wen, M. Wei, V. Yeddu, M. I. Saidaminov, Y. Gao, X. Luo, Y. Wang, H. Gao, C. Zhang, J. Xu, J. Zhu, E. H. Sargent, H. Tan, *Nat. Energy* **2020**, *5*, 870.
[26] Y. Fang, A. Armin, P. Meredith, J. Huang, *Nat. Photonics* **2019**, *13*, 1.
[27] Y. Zhao, C. Li, J. Jiang, B. Wang, L. Shen, *Small* **2020**, *16*, 2001534.
[28] N. Ma, J. Jiang, Y. Zhao, L. He, Y. Ma, H. Wang, L. Zhang, C. Shan, L. Shen, W. Hu, *Nano Energy* **2021**, *86*, 106113.
[29] R. Ollearo, J. Wang, M. J. Dyson, C. H. L. Weijtens, M. Fattori, B. T. van Gorkom, A. van Breemen, S. C. J. Meskers, R. A. J. Janssen, G. H. Gelinck, *Nat. Commun.* **2021**, *12*, 7277.
[30] C. Zou, Z. Zhou, X. Liu, F. Zhang, J. Xie, Y. Su, S. Yang, Y. Hou, *Adv. Opt. Mater.* **2022**, *10*, 2201769.
[31] F. Liu, K. Liu, S. Rafique, Z. Xu, W. Niu, X. Li, Y. Wang, L. Deng, J. Wang, X. Yue, T. Li, J. Wang, P. Ayala, C. Cong, Y. Qin, A. Yu, N. Chi, Y. Zhan, *Adv. Sci.* **2023**, *10*, 2205879.
[32] L. He, G. Hu, J. Jiang, W. Wei, X. Xue, K. Fan, H. Huang, L. Shen, *Adv. Mater.* **2023**, *35*, 2210016.
[33] V. D. Mihailetchi, J. Wildeman, P. W. Blom, *Phys. Rev. Lett.* **2005**, *94*, 126602.
[34] M. T. Xiong Gong, Y. Xia, W. Cai, J. S. Moon, Y. Cao, G. Yu, C.-L. Shieh, B. Nilsson, A. J. Heeger, *Science* **2009**, *325*, 1665.
[35] C. Bao, J. Yang, S. Bai, W. Xu, Z. Yan, Q. Xu, J. Liu, W. Zhang, F. Gao, *Adv. Mater.* **2018**, *30*, 1803422.